CCIT Report #454
November 2003

Clear Underwater Vision

Yoav Y. Schechner and Nir Karpel
Department of Electrical Engineering, Technion - Israel Institute of Technology
Technion City, Haifa 32000, Israel
yoav@ee.technion.ac.il, karpeln@tx.technion.ac.il

Abstract

Underwater imaging is important for scientific research and technology, as well as for popular activities. It increasingly benefits from computer vision. In this work, we present a computer vision approach which easily removes degradation effects in underwater vision. We analyze the physical effects of visibility degradation. We show that the main degradation effects can be associated with partial polarization of light. We therefore present an algorithm which inverts the image formation process, to recover a good visibility image of the object. The algorithm is based on a couple of images taken through a polarizer at different orientations. As a by product, a distance map of the scene is derived as well. We successfully used our approach when experimenting in the sea using a system we built. We obtain great improvements of scene contrast and color correction, and nearly doubled the underwater visibility range.

1 Underwater Vision

Underwater imaging is widely used in scientific research and technology. Computer vision methods are being used in this mode of imaging for various applications [3, 32, 35], such as mine detection, inspection of underwater power and telecommunication cables, pipelines [11, 27], nuclear reactors, and columns of offshore platforms [11]. Underwater computer vision is commercially used to help swimming pool life guards [19]. As in conventional computer vision, algorithms are sought for navigation and control [36] of submerged robots. In addition, underwater imaging is used for research in marine biology [1, 14, 30, 35], archaeology [2, 16] and mapping [36]. Moreover, underwater photography [34] is becoming more accessible to the wider public.

Underwater vision is plagued by poor visibility conditions [12, 15, 17, 32, 35]. According to Ref. [11], most computer vision methods (e.g., those based on stereo triangulation or on structure from motion) cannot be employed directly underwater. This is due to the particularly challenging environmental conditions, which complicate image matching and analysis. It is therefore important to alleviate these visibility problems. What makes underwater imaging media so problematic? To understand the challenge, consider

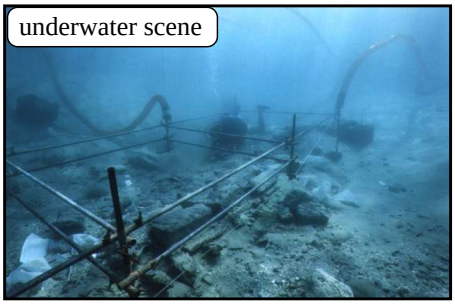

Figure 1. An underwater archaeological site. The visibility and colors quickly degrade as a function of distance.

Fig. 1, which shows an underwater archaeological site about 2.5 meters deep. It is easy to see that visibility degradation effects vary as distances to the objects increase [15]. Since objects in the field of view are at different distances from the camera, the *causes* for image degradation are spatially varying. This situation is analogous to open-air vision in bad weather (fog or haze), described in Refs. [5, 23, 24, 26]. Contrary to this fact, traditional image enhancement tools, e.g., high pass filtering and histogram equalization are typically spatially invariant. Since they do not model the spatially varying distance dependencies, traditional methods are of limited utility in countering visibility problems, as has been demonstrated in experiments [24, 26].

In this work we develop a physics-based approach for recovery of visibility when imaging underwater scenes in natural illumination. Since it based on the models of image formation, the approach automatically accounts for dependencies on object distance, and estimates a distance map of the scene as a by-product. The approach is fast, and it relies on raw images taken through different states of a *polarizing filter*.[1] These raw images have slight photometric differences. These differences serve as initial cues for algorithms that factor out turbidity effects. The work is inspired by recent computer vision methods, that were devised to recover open-air scenes (not underwater) degraded by atmospheric haze or fog [23, 24, 29, 26]. It is also interesting to note that marine animals use polarization for improved vision [30, 35].

Some methods improve underwater visibility by using

[1] Polarization filtered images have been used in various computer vision algorithms dealing with reflections [10, 25, 28, 35]. These methods evolved along with developments of polarimetric imaging devices [7, 8, 35].

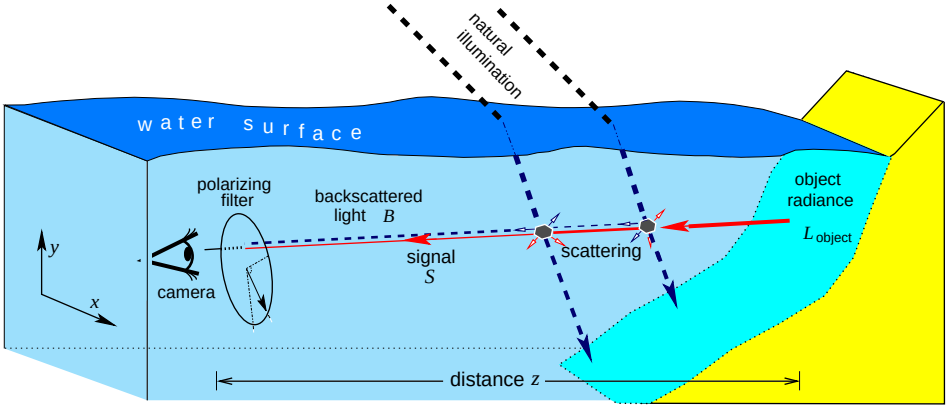

Figure 2. Underwater imaging of a scene, e.g., a reef, through a polarizing filter. [Dashed rays] Light coming from a source is backscattered towards the camera by particles in the water. The backscatter increases with the distance z to the object. [Solid ray] Light emanating from the object is attenuated and somewhat blurred as z increases, leading to the signal S. Without scattering and absorption along the line of sight (LOS), the object radiance would have been L_{object}.

specialized active radiation hardware [12, 15, 17]. In contrast, we deal with a passive computer vision approach, exploiting natural illumination. Another prior approach is based on a simple subtraction of the differently polarization filtered images [8, 12], or displays the degree of polarization (DOP) [9, 32]. That approach has fundamental disadvantages. It assumes that polarization is associated with the object radiation, rather than the causes which degrade this signal. However, due to depolarization, this assumption becomes invalid as distances increase. Moreover, such enhancement methods are far from inverting the image formation process and recovering the objects. In contrast, our approach inverts the physical model, thus the recovered image is similar to clear visibility appearance. Our approach is based on a *fact* [18, 22]: in natural illumination, underwater polarization is associated with the prime visibility disturbance which we wish to delete (termed *backscatter*).

To demonstrate the approach, we built an underwater polarization imaging system composed of both custom and off-the-shelf components (the considerations for selecting the components are described). We used the approach by experimenting in the sea. Significant improvements of contrast and color are obtained. The recovered range map indicates that the visibility range has been approximately doubled, thanks to the approach.

2 Theoretical Background

As depicted in Fig. 2, when imaging underwater we sense two sources. The first source is the scene object at distance z, whose radiance is attenuated by absorption and scattering in the water. It is also somewhat blurred. The image corresponding to this degraded source is the *signal*. The second source is the ambient illumination. Part of that light is scattered towards the camera by the particles in the water. It is termed *backscattered light* in literature dealing with underwater optics [15, 21, 22], and is analogous to the airlight phenomenon in atmospheric imaging [23, 24]. This section describes each of these components.

2.1 The Signal

2.1.1 Direct Transmission

The signal is composed of two components, termed *direct transmission* and *forward scattering* [15, 21, 22]. This section details the direct transmission, while the next section describes forward scattering. As a light ray progresses from the object towards the camera, part of its energy is lost due to scattering and absorption. The fraction which does reach the camera is the direct transmission[2], given by

$$D = L_{\text{object}} e^{-\eta z} \quad , \tag{1}$$

where η is the attenuation coefficient. Here L_{object} is the object radiance we would have sensed, had there been no scattering and absorption along the line of sight (LOS).

The attenuation coefficient is given by $\eta = \alpha + \beta$, where α is the absorption coefficient and β is the total scattering coefficient of the water. The scattering coefficient β expresses the ability of an infinitesimal water volume to scatter flux in all directions. Integrating over all solid angles $\vec{\Theta}$,

$$\beta = \int_{\vec{\Theta}} \beta(\vec{\Theta}) d\Omega = 2\pi \int_0^{\pi} \beta(\theta) \sin(\theta)\, d\theta \quad , \tag{2}$$

where θ is the scattering angle relative to the propagation direction. The angular scattering coefficient $\beta(\theta)$ is sometimes referred to as the $phase\ function$. Note that the variables $\alpha, \beta(\theta), \eta$ and L_{object} are all functions of the wavelength λ.

2.1.2 Forward Scattering

The forward scattering component is similar to the direct transmission. However, it represents light scattered forward at small angles relative to LOS. This creates image blur given by the convolution

$$F = D * g_z \quad , \tag{3}$$

[2] There is a proportion factor between the scene radiance and image irradiance that depends on the imaging system, but does not depend on the medium and its characteristics.

where D is given by Eq. (1) and g_z is a point spread function (PSF). The PSF is parameterized by the distance z, since the farther the object, the wider the support of the blur kernel.

There are several models in the literature for the form of the underwater PSF [21, 33]. Since the PSF depends on the hydrsols floating in the water, the models are typically parameterized by various empirical constants. For example, the model in Refs. [15, 21] is of the form

$$g_z = \left(e^{-\gamma z} - e^{-\eta z}\right) \mathcal{F}^{-1}\left\{G_z\right\} \text{ where } G_z = e^{-Kz\omega} \quad (4)$$

while $K > 0$ and γ are empirical constants, $\mathcal{F}^{-1}$ is the inverse Fourier transform, and ω is the spatial frequency in the image plane. Note that G_z is a low pass filter. The effective frequency "width" of G_z is inversely proportional to z. This expresses the increase of spatial blur spread for distant objects. The constant γ is limited to $|\gamma| \leq \eta$ [21]. It is important to note that the models of the PSF obtained empirically and through numerical simulations [21, 33] do not conserve energy as light propagates in z. This is clearly the case in Eq. (4). Thus forward scattering is a blurred and attenuated version D.

Accounting for both the direct transmission (1) and the forward scattering (3), we define the *signal* as

$$S = D + F \quad . \quad (5)$$

We define an *effective object radiance* $L_{\text{object}}^{\text{effective}}$ as

$$L_{\text{object}}^{\text{effective}} = L_{\text{object}} + L_{\text{object}} * g_z \quad . \quad (6)$$

It is a somewhat blurred version of L_{object}. From Eqs. (1,3,5), the signal is

$$S = e^{-\eta z}\, L_{\text{object}}^{\text{effective}} \quad . \quad (7)$$

2.2 Backscattered Light

Backscatter does not originate from the object on the LOS. Rather, light coming from ambient illumination sources is scattered towards the camera (Fig. 2). The LOS is naturally lit mostly from the water surface above. In addition, the LOS is illuminated by the ground and by scattering particles in the surrounding water volume. Before integrating all the contributions, let us first analyze the effect of a single distant source.

The source illuminates the particles on the LOS from direction $\vec{r} = (\theta, \varphi)$ relative to the LOS, with intensity I^{source}. Following Refs. [15, 21], the contribution of this source to the backscatter is

$$B\left(\vec{r}\right) = \int_0^z \beta\left(\theta\right) I^{\text{source}}\left(\vec{r}\right) e^{-\eta l} [1 - f/(l + l_0)]^2 dl \quad (8)$$

where f is the focal length of the camera and l_0 is the distance between the lens and the underwater housing window. This integral accounts for scattering into the LOS at some distance l, followed by attenuation until reaching the camera. It also accounts for geometric projection of the irradiance on the detector, via the ratio $f/(l + l_0)$.

In practice, we can simplify Eq. (8), because typically $f/(\eta^{-1} + l_0) \ll 1$. Consider typical ranges of values as $\eta^{-1} \in [3m, 10m]$ (according to [22]), $f \in [20mm, 50mm]$, $l_0 \approx 80mm$, and object distance in the order of meters. We assessed the integrals numerically. It can be shown that to an accuracy of 98%, we can write Eq. (8) as

$$B(\vec{r}) \approx c\beta(\theta) I^{\text{source}}(\vec{r}) \int_0^z e^{-\eta l} dl \quad (9)$$

where $c = 1.08$. Solving the integral yields

$$B(\vec{r}) = B_\infty(\vec{r}) \left(1 - e^{-\eta z}\right) \quad , \quad (10)$$

where

$$B_\infty(\vec{r}) \equiv c I^{\text{source}}(\vec{r}) \beta(\theta) \quad (11)$$

is the backscatter in a LOS which extends to infinity in the water. Summing up the contribution from light sources at all directions, the total backscatter is

$$B = \int_{\vec{r}} B(\vec{r}) d(\vec{r}) = B_\infty \left(1 - e^{-\eta z}\right) \quad , \quad (12)$$

where

$$B_\infty \equiv \int_{\vec{r}} B_\infty(\vec{r}) d\vec{r} \quad (13)$$

is a scalar which depends on λ.

It is simple to show that a similar expression is obtained when generalizing to non-distant light sources (as particles in the water volume). This happens under the assumption that lighting does not vary along the LOS, or that such variations are practically integrated out. We believe that this is a reasonable assumption when imaging approximately horizontally, since natural underwater light comes from a limited light cone directly *above* [6, 14], and is thus typically unobscured along the LOS.

We now discuss the significance of backscatter in the image degradation. The total image irradiance is

$$I^{\text{total}} = S + B = e^{-\eta z}\, L_{\text{object}}^{\text{effective}} + B \quad . \quad (14)$$

To gain intuition about the contribution of each component, we performed a simulation of underwater imaging, whose results are shown in Fig. 3. The effects of water are simulated using a model for oceanic water [22] with a low concentration of chlorophyll and a moderate concentration of hydrosols. Fig. 3 shows a colorful set of objects with radiance L_{object}. Then it shows $L_{\text{object}}^{\text{effective}}$, which accounts for blur by forward scattering. Note that the colors change a little due to forward scattering, since Eq. (4) includes an attenuation factor, which is implicitly wavelength dependent. We simulated the effects of varying distances by setting a distance map to the scene: the distance linearly increases from 0.5m at the bottom of the image to 3.5m at its top.

The visibility strongly deteriorates at the image I^{total}, which incorporates backscatter[3] and attenuation effects. Now, even objects at moderate distances are swamped in a veiling blue light and become obscured. Backscatter affects the color and contrast also of the close objects. This

[3] The weight of the backscatter relative to the signal depends on the object albedo. The larger the albedo, the stronger the signal is. Based on empirical studies of typical terrestrial objects [13], we set the average albedo to 0.2 .

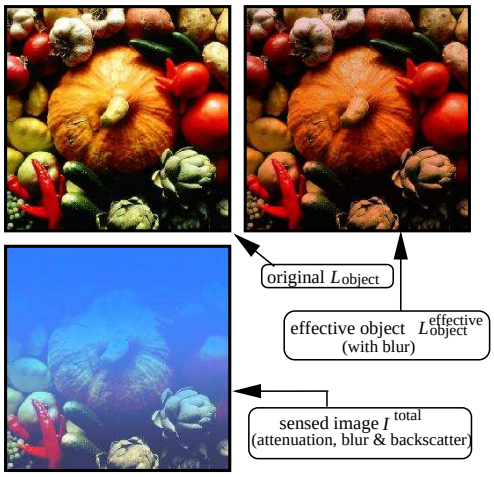

Figure 3. Simulating underwater imaging. The bottom part of the scene is set to be 0.5 meters away. The distance linearly changes to 3.5 meters at the top. We rendered the scene as if it is underwater, accounting for attenuation, blur (forward scattering) and backscatter. The latter effect is the prime cause for contrast degradation.

observation is consistent with analogous conclusions regarding airlight in the atmosphere. In the atmosphere, the airlight in daylight is the most prominent image component, much more than the signal [13] (except for very short distances). For this reason, the airlight is the most important contributor to aerial image degradation, rather than blur [26]. A similar conclusion applies underwater: backscatter is the major contributor to image degradation.

2.3 Polarization

Underwater scattering involves polarization effects. We exploit these effects to compensate for underwater visibility degradation, as we describe in the following sections. First, however, we describe the models for these effects. Consider a narrow source, which illuminates the scattering particles residing on the LOS. The narrow source and the LOS from the camera to the object define a plane of incidence. We divide the backscattered light into two polarization components that are *parallel* and *perpendicular* to this plane, $B^{\parallel}(\vec{r})$ and $B^{\perp}(\vec{r})$ respectively. Underwater the illumination distribution is rather predictable: its dominant direction lies within a cone around the vertical axis [6, 14]. For this reason, underwater *natural backscatter is typically partially* polarized horizontally [6, 14, 18].

In order to sense the different polarization components we image the scene through a polarizing filter (Fig. 2). Since natural backscatter is partially polarized, then its intensity depends on the filter's orientation around the optical axis. There are two orthogonal orientations of the polarizer for which its transmittance of the backscattered light reach extremum values $B^{\max}$ and $B^{\min}$. These are the two linear polarization components of the backscatter, i.e.,

$$B = B^{\max} + B^{\min} \quad , \tag{15}$$

where B is given by Eq. (12). The DOP of the backscattered light is defined by:

$$p \equiv \left(B^{\max} - B^{\min}\right)/B \quad . \tag{16}$$

As for the signal S, we assume that its polarization is insignificant relative to the backscatter, for three reasons. One reason for this assumption is the depolarized nature of reflection from rough surfaces. This particular reason is invalid in case of specular or other polarizing objects. Yet even in those cases the assumption still holds, for the remaining two reasons: multiple scattering along the LOS, and the intensity dominance of the backscatter over the signal. Multiple scattering of the signal along the LOS diminishes the original signal polarization as distance increases. In addition, the signal decreases (Eq. 7) while the backscatter (Eq. 12) increases with distance. Thus backscatter and its polarization dominate the measurements as distance increases. Therefore, as in atmospheric haze [29], the accuracy of the model increases where it is needed most - at distant objects, which are most affected by visibility degradation.

3 Image Acquisition

When a polarizer is mounted, the sensed intensity at each image pixel changes as a cosine function of the filter orientation angle. Similarly to backscattered light, there are two orthogonal polarizer angles corresponding to extremum values of the intensity, $I^{\max}$ and $I^{\min}$, where

$$I^{\text{total}} = I^{\max} + I^{\min} \quad , \tag{17}$$

where I^{total} is given by Eq. (14). Since we assume that the signal polarization is insignificant, the polarizer modulates only the backscatter. Therefore, the raw images corresponding to the exrema of the intensity measure

$$I^{\max} = S/2 + B^{\max} \quad \text{and} \quad I^{\min} = S/2 + B^{\min} \, . \tag{18}$$

Note that $I^{\min}$ is the image taken at the "best state" of the polarizer, where the disturbing backscatter is minimal. On the other hand, $I^{\max}$ is the image taken at the "worst state" of the polarizer, where the backscatter is maximal.

In order to acquire such images we built a custom system for underwater polarimetric imaging. Several specifications determined its design, as detailed in the Appendix. Based on that, we built the system shown in Fig. 4. The housing is commercially available. For the reasons explained in the Appendix, we close the housing with a *dome* port made of *glass*, while a *circular* polarizer is attached *externally* to it. The surrounding water flows to the space between the external polarizer and the dome, through several openings in the housing's interface to the polarizer mount. We use the Nikon D100 digital SLR camera, which allows for raw output data having a linear response (i.e., no gamma correction) without white balancing.[4]

[4] We confirmed the linear response of the system using different exposures of the MacBeth ColorChecker calibration chart.

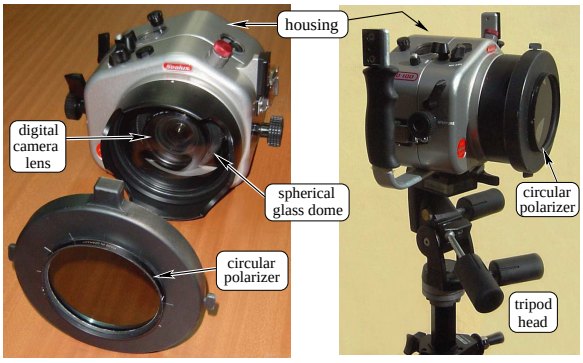

Figure 4. The imaging system we used. [Left] With the polarizer mount separated, the dome and lens are visible. [Right] The complete system mounted on a tripod.

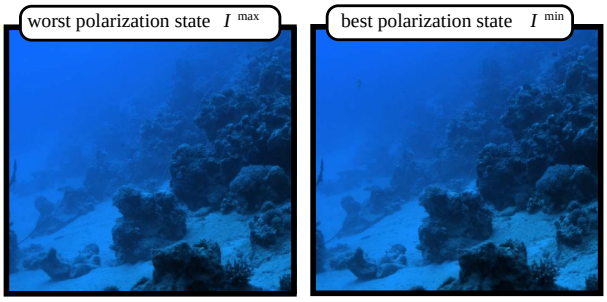

Figure 5. An underwater scene 26m below the water surface. The images were taken using horizontal and vertical polarizer orientations. Both images are contrast stretched, yet their visibility is poor. Their difference is hardly noticeable.

We scuba-dived to a depth of 26 meters in a sea containing coral reefs. We took images at the two states of the polarizer. The raw images[5] are shown in Fig. 5. Both of the images have a very low contrast, yet their slight differences provid the key for substantial visibility improvement by a mathematical algorithm, described next.

4 Clear Underwater Visibility

The algorithm for overcoming the underwater visibility degradation has similarities to dehazing methods for aerial images, described in [23, 24, 29]. For this reason, we use the adjective *dehazed* to describe the image resulting from the algorithm, although haze is certainly not the proper word to use for underwater effects. In addition to "dehazing" we need to address the underwater illumination color bias. As we go deeper underwater, the red portion of the illumination spectrum is absorbed by the water [34]. Hence, for perceptual plausibility, we apply a white balancing procedure after we compensate for the effects occurring along the LOS.

[5] For clarity of display, the brightness of the displayed pictures in this paper underwent a standard contrast enhancement (stretching), while their hue and color saturation were untouched. The recovery algorithms, of course, used the raw (not enhanced) images.

4.1 Recovering the Object Radiance

Assume for a moment that we have an estimate of the global parameters B_∞ and p. From Eqs. (15,16,18), we estimate the backscatter as

$$\hat{B} = (I^{\max} - I^{\min})/p \ . \tag{19}$$

Inserting this estimate into Eqs. (12,14,17), we obtain an estimate for the "dehazed" object radiance

$$\hat{L}^{\text{effective}}_{\text{object}} = (I^{\text{total}} - \hat{B})/\hat{t} \quad \text{where} \quad \hat{t} = 1 - \hat{B}/B_\infty \ . \tag{20}$$

Here $\hat{t}$ is the estimated water transmittance, which is related to the object distance z by

$$\hat{t} = e^{-\eta z} \ . \tag{21}$$

We process each color channel independently this way.

The "dehazed" image is an estimate of $L^{\text{effective}}_{\text{object}}$. We therefore do not compensate for image blur, but only for the veiling effect of backscatter, and for attenuation. At this point we make do with this estimate. The reason stems from the discussion in Sec. 2.2: backscatter is the prime reason for image contrast degradation, hence overcoming backscatter, rather than blur, is the prime step for clearing visibility. Note that the dehazed images is a result of inversion of the image formation process. It therefore represents a recovery of the object, in contrast to methods which apply ad-hoc expressions of the DOP [4] for image enhancement.

To perform this recovery we need estimates of the global parameters B_∞ and p. These are intrinsic parameters of the water and lighting. This estimation is similar to algorithms which had been developed for open-air imaging [23, 29]. We obtain these estimates by measuring pixels corresponding to objects "at infinity", i.e., which are so distant inside the water, that their signals are negligible due to attenuation. In this regard, the estimation underwater is easier than in the atmosphere, since the visibility range underwater is very short. Therefore, there are usually plenty of horizontal viewing directions in which no object is visible.

We ran this algorithm on the raw images shown in Fig. 5. In Fig. 6, the "dehazed" image is shown in conjunction a region of the best raw image. The dehazed image indeed has a better contrast, it shows details that are not seen in the input photographs, and better shows the far objects. The colors, however, remain very biased towards the blue. The reason for this is that at this depth under the water surface, the red component of the illumination has lost most of it energy.

4.2 Compensating for Illumination Color

To compensate for the illumination blue color bias, we performed a simple white-balancing operation on the images *after* being processed for dehazing. Knowing that the sand in that diving site it rather white, we normalized the color of each image by the color of a sandy patch in the field of view. We must note that this multiplicative normalization compensates only for the illumination color, but not for the additive backscatter. For this reason, the white patch should

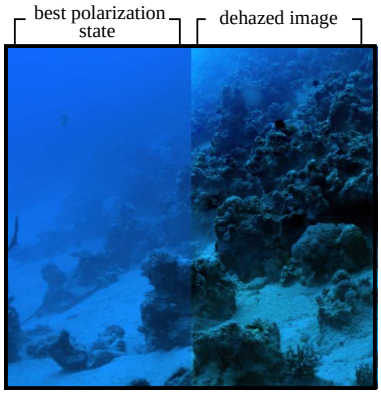

Figure 6. Comparison between the best raw image (left) and the "dehazed" image (right). The dominant hue is blue due to the spectrum of the illumination reaching deep below the water surface.

be measured as close as possible to the camera, where the backscatter is minimal. We therefore measured the color of a sandy patch at the *bottom* of the picture, where it is closest.

We performed this process independently on the "dehazed" image and on $I^{\min}$. In analogy to Fig.6, portions of both color-corrected images are shown in Fig.7. It is now clear that the dehazed image has a much improved contrast and color. The ability to see objects of orange hue in *natural* illumination at such an underwater depth is remarkable [34]. White balancing improves the raw polarized image (left side of Fig.7), to a lesser degree. The reason is that in the raw image the backscatter is very significant, especially as distances increase. The backscatter is not compensated by white balancing, thus it persists in its degradation of the raw image.

5 How Far Do We See?

We are interested in a *quantitative* estimate for the visibility improvement. A common visibility criterion is the visibility range, i.e., at which distance we may still observe certain details. Therefore, in this section we deal with the aspects of this criterion.

As a by-product of the radiance recovery process, we get an estimate of the distance map of the scene. From Eq. (21) The distance z is estimated as a function of (x, y) up to a global scale factor η . It is given by

$$\widehat{\eta z}(x,y) = -\ln[1 - \hat{B}(x,y)/B_{\infty}] \quad , \tag{22}$$

and shown in Fig. 8. We do not know what the attenuation coefficient η is. Nevertheless, we can quantitatively determine the *relative distances* in the scene. For example, when comparing two image regions, we can determine that one of them is, say, three times as distant from the camera as the other one. This fact enables assessing the ratio of improvement of the visibility range, which is achieved by the "dehazing" method.

To calculate the ratio of visibility ranges, we should compare the appearance of the same object at different distances.

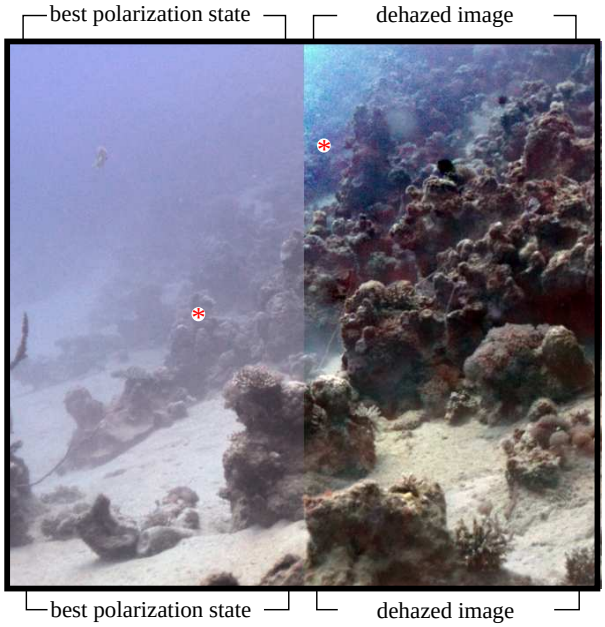

Figure 7. Comparison between the best raw image and the "dehazed" image. These images underwent white balancing based on a close white sand patch. For the "best polarized" image this process quickly loses its effectiveness as object become more distant. In the "dehazed" image colors are recovered to large distances. [Marked Points]: The regions around the points have the same contrast in their respective images. However, the point in the "dehazed" image part is twice as distant as the one in the raw image part, indicating the increase of visibility range.

For a rough estimate, we selected from the scene two regions which have the following characteristics:

• Both regions have a similar object content.

• The contrast level of one region in the raw image, matches the contrast of the second region in the dehazed image.

The selected regions are around the marked points in Fig. 6. Both regions contain the same type of objects: chunks of the coral reef. We therefore assume that the intrinsic object properties are the same in these two regions.

The contrast of the left marked region in raw image is the same as the contrast of the right marked region in the dehazed image. To make this claim, we use a generalized definition of contrast at a region. The intensity contrast between two points $k = 1, 2$ is defined by $|I_1 - I_2|/|I_1 + I_2|$. In a region having N pixels, we use

$$c = \mathrm{STD}\{I_k\} / \left(\Sigma_{k=1}^{N} I_k\right) \quad , \tag{23}$$

where $\mathrm{STD}\{I_k\}$ is the standard deviation of the N intensity values. In order to minimize the contribution of noise, Eq. (23) was estimated only in the blue channel, for which the signal to noise ratio is greatest.

To conclude, both regions have a similar object content. The contrast level of one region at a certain distance in the raw image, matches the contrast of the second region in the dehazed image, but at a longer distance. Using Eq. (22), the

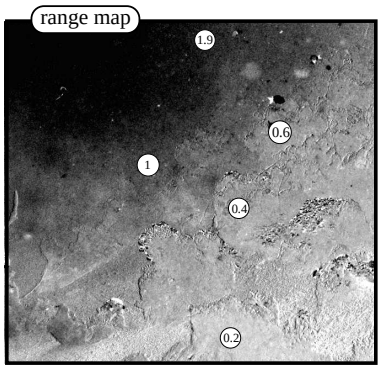

Figure 8. The estimated range map of the object. Longer distances are displayed at darker graylevels. The distance to some points is written in units of the attenuation distance η^{-1}.

range ratio between the points is 1.8. We therefore, conclude that the method demonstrated an increase of the visibility range by a factor of ≈ 2. We plan to follow up with more controlled experiments using standard calibration targets.

6 Discussion

We presented a method that can overcome degradation effects occurring in underwater vision. It is based on simple analysis of images acquired through a polarizing filter. Since it is physics-based, the method also recovers information about the scene structure (distances). We believe that this approach can lead to *useful* tools in underwater photography, underwater research, and underwater technological applications.

Appendix : Building an Underwater Polaricam

As mentioned in Sec. 3, there are several specifications needed for the underwater imaging system. They arise since we make *quantitative* photometric measurements with the polarizer. The camera should have a linear radiometric response and low noise. It should be housed in a watertight housing which withstands the pressures in the depths we work. In addition, there should be full control of the camera parameters (exposure time, aperture, etc.). Therefore, the housing should have mechanical controls which couple to these camera controls.

Optical Considerations

The main concern in the optical design is its affect on polarization. We use a polarizer to analyze the scene. However, we would like the *rest* of the optical system components to have *minimal effects* or sensitivities related to polarization. We achieve this by making the following decisions:

A dome port, or a flat port? The camera lens views the scene through a *port*, i.e., a transparent window in the housing [34]. Typical ports are flat or spherical. Consider Fig. 9. The chief ray from an object point in the water to the detector undergoes an angular deviation [34] at flat window interfaces. In this case, the window transmittance depends on

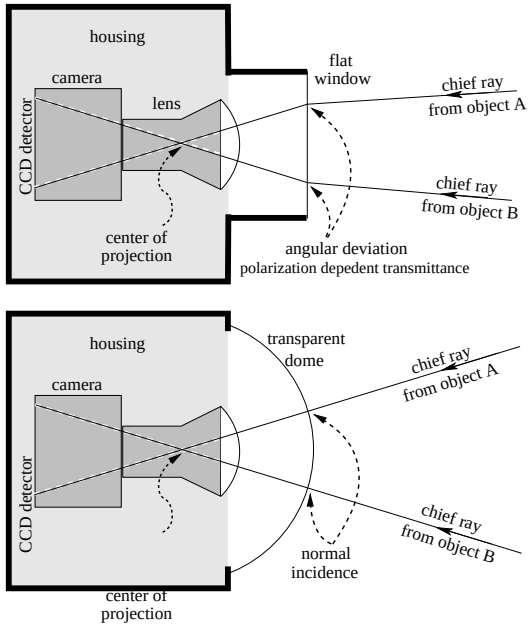

Figure 9. [Top] An unwanted effect: the transmittance of a flat port (window) is polarization dependent at oblique incidence. [Bottom] The preferred design: a spherical dome concentric with the center of projection eliminates this effect by creating normal incidence angles.

the polarization of the passing light [31]. This polarization dependence distorts the intensity readout values.

Dome ports, on the other hand, alleviate this problem. If the sphere's center coincides with the center of projection of the camera, then the chief ray from an object point to the detector is normal to the dome interface. At normal incidence the transmittance is independent of the linear polarization state [31]. For this reason, we decided to use a *dome port*.

An external or internal polarizer? Stress in the transparent port's material changes the polarization of the light it transmits. This effect is called the *photoelastic effect* [31]. Due to inhomogeneities in the material, this polarization effect is spatially varying. This spatially varies the transmittance though the polarizer, depending [31] on λ and the polarization state. Moreover, the effect may vary with the underwater depth, due to changes of the external water pressures.

In principle, placing the polarizer externally should eliminate visible photoelastic effects. We thus decided to place the polarizing filter *outside* the housing. The filter is thus the first optical component the light from the scene encounters as it enters the imaging system. The space between the external polarizer and the dome is filled with the water coming from the surroundings. In practice, the photoelastic visible effects are indeed greatly diminished, but not completely eliminated. Residual effects persist due to complicated refractions in the transparent port. To minimize such residual effects, we refer to the following considerations.

A glass dome, or a polycarbonate dome? The photoelastic

effect is much smaller in glass than in polycarbonate materials (plastics) [31]. We thus decided to use a *glass dome*.

A circular or linear polarizer? In practice, the dome may not be precisely concentric with the center of projection. In non-normal incidence, different polarization components are differently transmitted, affecting the intensity readouts. To counter this possibility, we decided to use a *circular polarizer*: it filters the linear polarization of its input (scene) while it outputs circular polarization [31] to the dome. In this case, the light transmittance of the dome is independent of the polarizer angle. Yet, circular polarizers are tuned to a narrow band (typically "green"), and do not perform perfectly across the spectrum. So, while this measure helps in minimizing unwanted polarization effects, the other considerations listed above should be employed as well.

Acknowledgments

We are grateful to Nadav Shashar for helpful discussions. We are also grateful to Yoav Failer for enabling the use of the Technion's swimming pool in preliminary experiments. We also wish to thank Naftalli Blau and Nir Geva for their help in the scuba dives. Yoav Schechner is a Landau Fellow - supported by the Taub Foundation, and an Alon Fellow. The work was supported by the Ollendorff Center in the Elect. Eng. Dept. at the Technion.

References

[1] J. Åhlén and D. Sundgren, "Bottom reflectance influence on a color correction algorithm for underwater images," Proc. SCIA, 922-926 (2003).

[2] R. D. Ballard, "Ancient Ashkelon," National Geographic Mag. **199**/1, 91-93 (2001).

[3] T. Boult, "DOVE: Dolphin omni-directional video equipment," Proc. IASTED Int. Conf. Robotics and Autom. 214-220 (2000).

[4] P. C. Y. Chang, J. C. Flitton, K.I. Hopcraft, E. Jakeman D. L. Jordan and J. G. Walker, "Improving visibility depth in passive underwater imaging by use of polarization,",App. Opt. **42**, 2794-802 (2003).

[5] F. Cozman and E. Krotkov, "Depth from scattering," Proc. CVPR, 801-806 (1997).

[6] T. W. Cronin and N. Shashar, "The linearly polarized field in clear, tropical marine waters: spatial and temporal variation of light intensity, degree or polarization and e-vector angle," J. Experim. Biol. **204**, 2461-2467 (2001).

[7] T. W. Cronin, N. Shashar and L. Wolff, "Portable imaging polarimeters," Proc. ICPR, Vol. 1 606-609 (1994).

[8] L. J. Denes, M. Gottlieb, B. Kaminsky and P. Metes, "AOTF polarization difference imaging," 27th AIPR Workshop: Advances Comp. Assist Recog., 106-115 (1998).

[9] N. Engheta, J. S. Tyo, M. P. Rowe and E. N. PughJr., "Biologically inspired polarization-difference imaging," 27^{th} Europ. Microwave Conf. & Exhibit. Vol. 2, pp. 978-983 (1997).

[10] H. Farid and E. H. Adelson, "Separating reflections and lighting using independent components analysis," Proc. CVPR, Vol. 1, 262-267 (1999).

[11] G. L. Foresti, "Visual inspection of sea bottom structures by an autonomous underwater vehicle," IEEE Trans. Syst. Man and Cyber, Part B **31**, 691-705 (2001).

[12] S. Harsdorf, R. Reuter and S. Tönebön, "Contrast-enhanced optical imaging of submersible targets," Proc. SPIE **3821**, 378-383 (1999).

[13] R. C. Henry, S. Mahadev, S. Urquijo and D. Chitwood, "Color perception throught atmospheric haze," J. Opt. Soc. Am. A **17**, 831-835 (2000).

[14] G. Horváth and C. Varjú, "Underwater refraction-polarization patterns of skylight percieved by aquatic animals through Snell's window of the flat water surface," Vision Research **35**, pp. 1651-1666 (1995).

[15] J. S. Jaffe, "Computer modeling and the design of optimal underwater imaging systems," IEEE J. Oceanic Engin. **15**, 101-111 (1990).

[16] Y. Kahanov and J. Royal, "Analysis of hull remains of the Dor D Vessel, Tantura Lagoon, Israel," Int. J. Nautical Archeology **30** 257-265 (2001).

[17] D. M. Kocak and F. M. Caimi, "Computer vision in ocean engineering," *The Ocean Eng. Handbook*, editor F. El-Hawari, Ch. 4.3 (CRC Press, 2001).

[18] G. P. Können, *Polarized light in nature*, 1-10,96-99,131-137,144-145 (Cambridge University Press, 1985).

[19] J. M. Lavest, F. Guichard and C. Rousseau, "Multiview reconstruction combining underwater and air sensors," Proc. IEEE Int. Conf. Image Process. vol. 3, 813-816 (2002).

[20] Y. Matsushita, K. Nishino, K. Ikeuchi and M. Sakauchi, "Shadow elimination for robust video surveilance," Proc. IEEE Worksh. Motion and Video Comp., 15-21 (2002).

[21] B. L. McGlamery, "A computer model for underwater camera system," Proc. SPIE **208**, 221-231 (1979).

[22] C. D. Mobley, *Light and Water: Radiative Transfer in Natural Waters*, Ch. 3,5 (Academic Press, San-Diego 1994).

[23] S. G. Narasimhan and S. K. Nayar "Vision and the atmosphere," Int. J. of Computer Vision **48**, 233-254 (2002).

[24] S. G. Narasimhan and S. K. Nayar "Contrast restoration of weather degraded images,", IEEE Trans. PAMI **25**, 713-724 (2003).

[25] S. K. Nayar, X. S. Fang and T. Boult, "Separation of reflection components using color and polarization," Int. J. Computer Vision **21**, 163-186 (1997).

[26] J. P. Oakley, "Improving image quality in poor visibility condiitons using a phusical model for contrast degredation," IEEE Tran. on image processing. **7**, 167-179 (1998).

[27] A. Ortiz, M. Simo and G. Oliver, "A vision system for an underwater cable tracker," Machine Vis. and App. **13**, 129-140 (2002).

[28] M. Saito, Y. Sato, K. Ikeuchi, and H. Kashiwagi, "Measurement of surface orientations of transparent objects by use of polarization in highlight," JOSA A **16**, 2286-2293 (1999).

[29] Y. Y. Schechner, S. G. Narasimhan and S. K. Nayar "Instant dehazing of images using polarization," Proc. IEEE CVPR, Vol. I, 325-332 (2001).

[30] N. Shashar and T. S. Cronin, "Polariazation contrast vision in octopus," J. Exper. Biol. **199**, 999-1004 (1996).

[31] W. A. Shurcliff and S. S. Ballard, *Polarized light*, pp. 98-103,120-121 (Van Nostrand Co., Princeton, 1964).

[32] J. S. Talyor, Jr., and L. B. Wolff "Partial polarization signature results from the field testing of the SHallow water Real-time IMaging Polarimeter (SHRIMP)," MTS/IEEE Oceans, Vol. 1, 107-116 (2001).

[33] K. J. Voss, "Simple empirical model of the oceanic point spread function," ,App. Opt. **30**, 2647-51 (1991).

[34] M. Webster *The art and technique of underwater photography*, pp. 19-22,33-39,146-149 (Fountain Press, Surray 1998).

[35] L. B. Wolff, "Polarization vision: a new sensory approach to image understanding," Image & Vision Comp. **15** 81-93 (1997).

[36] X. Xu and S. Negahdaripour, "Automatic optical station keeping and navigation of an ROV: sea trial experiment," IEEE Marine Technol. Soc. Part, vol.1,pp.71-6 (1999).